Cryogenic shear layers: experiments and phenomenological modeling of the initial growth rate under subcritical and supercritical conditions

B. Chehroudi [a,*], R. Cohn [b], D. Talley [b]

[a] *Engineering Research Consultants Inc., 10 E. Saturn Blvd., Edwards AFB, CA 93524-7680, USA*
[b] *Air Force Research Laboratory (AFRL), Space and Missile Propulsion Division, AFRL/PRSA, 10 E. Saturn Blvd, Edwards AFB, CA 93524-7680, USA*

Abstract

A jet of a cryogenic fluid, typically liquid N_2, is injected into a chamber whose ambient pressure is varied to values exceeding the critical pressure of the injectant. The structure of the jet and the shear layer between the jet and the ambient have been examined. Results from visualization, jet initial growth rate, fractal analysis, and Raman scattering measurements indicate that the behavior of the injected fluid changes from liquid spray-like to gaseous jet-like behavior as pressure increased. This is attributed to the reduction of the surface tension and enthalpy of vaporization as the critical pressure of the injectant is approached. The initial divergence angle indicating the growth rate of the jet is measured at the jet exit. These values are then compared with those measured from a large number of other mixing layer flows, including atomized liquid sprays, turbulent incompressible gaseous jets, supersonic jets, and incompressible but variable density jets covering over four orders of magnitude in the gas-to-liquid density ratio, the first time such a plot has been reported over this large a range of density ratios. At and above the critical pressure of the injected fluid, the jet initial growth rate measurements agrees well with the theory and measurements of incompressible, variable density, gaseous mixing layers. This is the first time a quantitative parameter has been used to demonstrate that the similarity between the two flows extends beyond mere qualitative physical appearance. The initial growth rate using Raman scattering is also in reasonably good agreement with our measurements using shadowgraphy if twice the FWHM of the normalized intensity radial profiles are used. Finally, an equation based on a proposed physical mechanism combined with the characteristic gasification time (τ_g) and interfacial bulge formation/separation time (τ_b) is proposed, $\theta = 0.27[\tau_b/(\tau_b + \tau_g) + (\rho_g/\rho_l)^{0.5}]$, that shows good agreement with the measured initial growth rate data. It is found that the transition point from sub- (liquid-jet like) to supercritical (gas-jet like) behavior occurs when the time scale ratio ($\tau_b/(\tau_b + \tau_g)$) is approximately equal to 0.5. © 2002 Published by Elsevier Science Inc.

1. Introduction

In recent years, combustion chamber operating pressures have been increased in order to realize performance and/or efficiency benefits in a wide range of propulsion and energy conversion applications. In some cases, this has resulted in the injected fluid(s) experiencing ambient pressures exceeding their thermodynamic critical pressure(s). An example of particular interest in rocket applications is the cryogenic liquid hydrogen/liquid oxygen Space Shuttle Main Engine in which the combustion or thrust chamber pressure is about 22.3 MPa. Thrust chamber pressures for the Vulcain (Ariane 5) engine have been recorded to reach up to 10 MPa. Both of these pressures exceed the critical pressure of oxygen ($P_{cr} = 5.043$ MPa). In these applications, the initial temperature of the oxygen is below its critical temperature ($T_{cr} = 154.58$ K), and then undergoes a transition to a supercritical temperature as the oxygen is mixed and burned in the combustion chamber.

For single component fluids, the distinct difference between the gas and liquid phases disappears when either the pressure exceeds the critical pressure or the temperature exceeds the critical temperature. Near the critical point, the surface tension and enthalpy of vaporization vanish. Large variations in the density, thermal conductivity, and mass diffusivity also occur. For multicomponent fluids, the solubility of the gas phase in the liquid phase increases as pressure approaches the critical pressure, and mixture effects need to be taken into account in calculating the critical properties. The critical

---

* Corresponding author.
E-mail address: bruce.chehroudi@edwards.af.mil (B. Chehroudi).

properties of mixtures are referred to as the "critical mixing temperature" and the "critical mixing pressure" (Bruno and Ely, 1991). The critical mixing pressure can be many times the critical pressure of the individual components as seen in Woodward and Talley (1996).

Previous efforts, (for example, Newman and Brzustowski, 1971; Mayer et al., 1996), have reported a gas-like jet visual appearance at a supercritical chamber temperature and pressure with no evidence of droplets. Newman and Brzustowski (1971) studied steady CO_2 jets injected into a chamber of pure N_2 and also mixtures of $CO_2 + N_2$ at both sub- and supercritical pressures and temperatures. They explained the effects of increased chamber temperature on the jet appearance to be due to the progressive reduction in ambient gas density, the reduction in surface tension to zero at the critical temperature, and the increase in liquid CO_2 evaporation. Based on coarse photographs, they proposed the possibility of jet gasification, namely that at supercritical temperatures and pressures the jet could be treated as a variable-density single-phase turbulent submerged gas jet. Mayer et al. (1998) studied liquid cryogenic N_2 (LN_2) jets at a fixed temperature of 105 K injected into a N_2 environment at 300 K, but at varying ambient sub- to supercritical pressures, and observed drastic changes in the jet structure near and above the critical pressure. They attributed this behavior to a continual decline of surface tension until it vanished at and above the critical pressure. They also studied the coaxial injection, similar to the injection scheme used in cryogenic rocket engines, of LN_2 (at 97 K) inside gaseous He (at 280 K), as simulant fluids for H_2 and O_2. As before, changes in the jet structure were clearly observed as pressure increases were clearly observed. Again, these changes were attributed to increases in the solubility of He into N_2 and reductions in the surface tension. Finally, they studied H_2/O_2 combustion in a windowed model rocket combustion chamber, and again observed structural changes in the jet with pressure in both the ignition and steady state combustion phases. No evidence of droplets was observed at supercritical conditions.

Woodward and Talley (1996) studied the injection of LN_2 jets into gaseous N_2 and gaseous mixtures of N_2 and He at much lower Reynolds numbers than the above studies. For N_2/N_2 systems, observation of the resulting fluid structures at and above the critical pressure showed strong evidence that surface tension becomes negligibly small either at the instant of mass injection or very rapidly thereafter. Adding gaseous He (∼20 wt.%), however, was found to produce structures which again showed strong evidence of having surface tension at pressures up to twice the critical pressure of pure N_2, demonstrating the strong effect of composition on the critical mixing properties.

Anderson et al. (1995), Decker et al. (1998), Oschwald and Schik (1999), Oschwald et al. (1999), and

Chehroudi et al. (2000) used Raman scattering to investigate the structure of a cryogenic nitrogen jet under supercritical conditions. Decker et al. (1998) observed a smooth transition from the high-density core of a cryogenic, N_2 jet to the more rarefied, warmer N_2 in the ambient outer region. There was no distinct phase interface. The density radial profile was never observed to have a top hat profile, even as close as 2.5 injector diameters from the outlet. Based on limited tests, they concluded that the thermodynamic state of an injected supercritical fluid was of prime importance in determining the jet growth, and not the injection velocity or momentum.

The objective of this paper is to concisely present the experimental and modeling experiences gained thus far at AFRL on the injection of cryogenic fluids under subcritical to supercritical pressures. The structural features of the jet and the shear layer between the jet and the ambient will be described. An initial attempt to model the measured growth rates of the jet shear layer is also presented.

2. Experimental apparatus

Fig. 1 shows a schematic diagram of the experimental rig. The stainless steel chamber can withstand pressures and temperatures of up to 20 MPa and 473 K, respectively. It has two facing circular sapphire windows with two UV-grade side-mounted slot-shaped quartz windows for optical diagnostics and laser illumination of the chamber. Liquid N_2 is used to cool and/or liquefy the injectant passing through the cryogenic cooler prior to injection. The mass flow rate of the injectant is measured and regulated via a mass flowmeter, and a precision micrometer valve. Back-illumination of the jet is accomplished with diffuse light flashes (0.8 µs duration). A model K2 Infinity long distance microscope is used with a TM-745E high resolution (768(H) × 493(V) pixels in 8.8(H) × 6.6(V) mm actual sensing area) interlaced CCD camera by PULNix to form images of the injected jets. The resolution of this setup is 30 ± 7 µm. For the results reported, the cryogenic jet is injected through a sharp-edged stainless steel tube with a length, $l = 50$ mm, and inner and outer diameters measuring $d_e = 0.254$ mm and $d_o = 1.59$ mm respectively. This results in $l/d_e = 200$, which is sufficient to ensure fully developed turbulent pipe flow at the exit plane. The Reynolds number in these studies ranges from 25,000 to 70,000. The rig is fully instrumented to measure pressure, temperature, and mass flow rate of the injected fluid.

For the Raman scattering experiments, a Contunuum Powerlite 8010 frequency-doubled Nd:Yag pulsed laser (532 nm output wavelength) with a pulse energy of
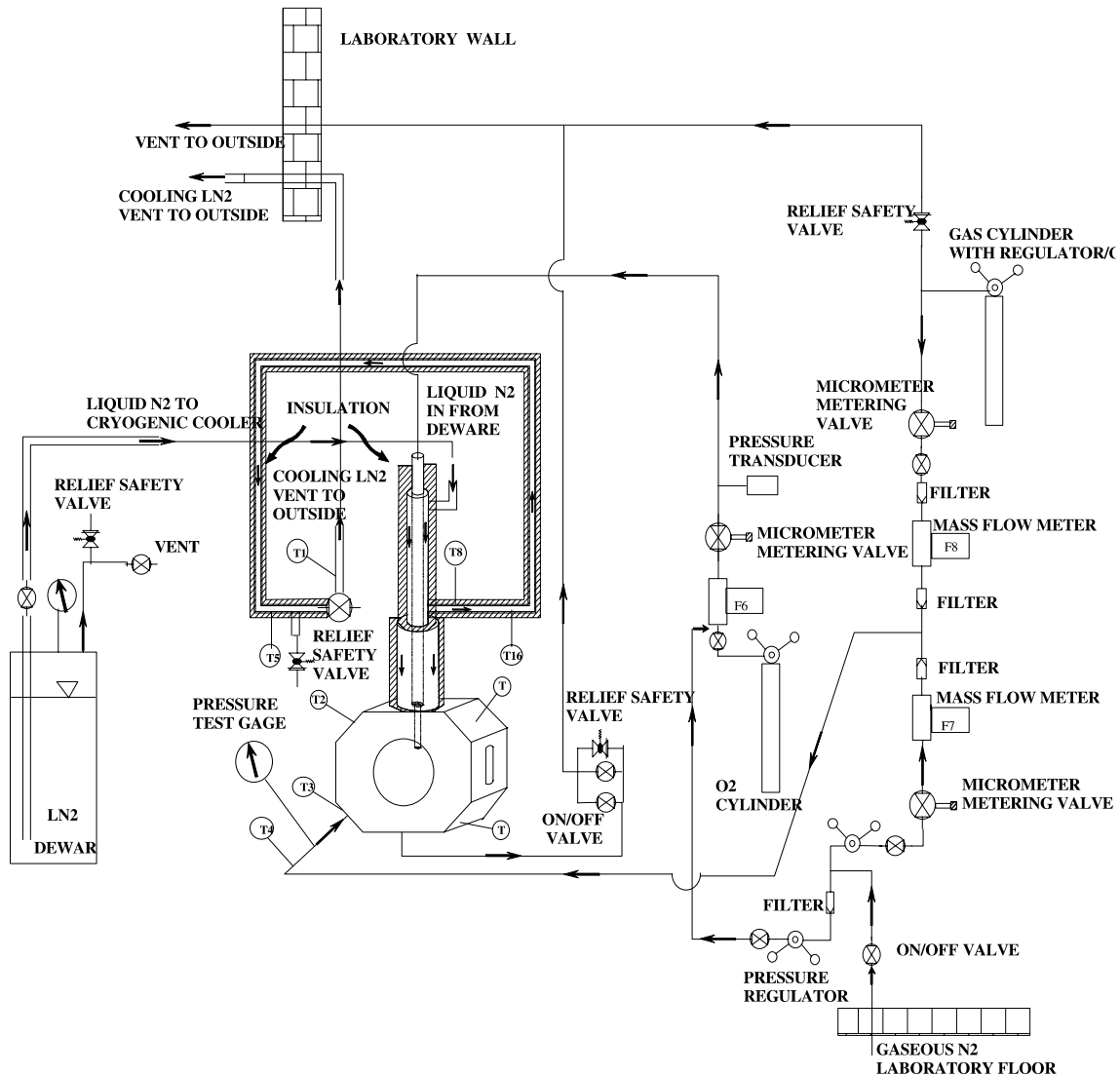
Fig. 1. Schematic diagram of experimental setup for sub- to supercritical jet injection.

330 mJ/pulse as a source to induce the Raman effect. The pulse repetition rate for this laser is 10 Hz with a pulse width of 10 ns. A passive pulse stretcher is designed to reduce the possibility of plasma formation. The original pulse is extended in time by dividing it into three major pulses, each being 10 ns in duration, but delayed in time by 8 and 16 ns. This results in a final pulse duration of about 26 ns. The laser beam is shaped by passing through a Galilean beam expander before forming a thin sheet via two cylindrical lenses. The laser sheet thickness was measured using an attenuator attached to a CCD camera and found to be about 100 μm. The entire assembly is on a separate optical bench which can be traversed in both vertical and horizontal directions.

The scattered Raman signal at 607 nm is detected by a cooled 576×384 pixel ICCD camera from Princeton Instruments. A set of three filters is also used to separate the Raman signal from the 532 nm incident beam. A high-pass OG570 filter is used to reduce the light at 532 nm by more than 10^5 and at 607 nm by not more than 10%. A holographic supernotch plus filter attenuates the light at 532 nm by better than 10^6 while less than 20% at 607 nm. Finally, a 10 nm bandwidth interference filter centered at 610 nm reduces the scattered light at 532 nm by better than 10^4 while attenuating by about 0.5 at 607 nm. Therefore, an optical density of better than 15 is achieved at the 532 nm laser wavelength while the transmittance of the Raman signal is 0.36. This arrangement was found to be adequate to ensure the removal of stray light while passing sufficient Raman signal for detection. The lens package consists of a Nikon PK-12/14 extension ring connected to one end of a Noct-Nikkor 58 mm F/# (1.2–16) lens with a NIK-2734 close-up lens located in its front. For more detailed on experimental setup see Chehroudi et al. (2002, 1999, 2000).

3. Visual appearance changes in cryogenic jets and shear layers

Fig. 2 (top row) shows representative images of a jet of liquid nitrogen (LN_2) ($P_{cr} = 3.39$ MPa, $T_{cr} = 126.2$ K) injected at an initial temperature of 99–110 K into room temperature (300 K) gaseous nitrogen (GN_2). For the results presented here, the chamber pressure is normalized (or reduced) by the critical pressure of the pure fluid in the jet; P_r (i.e. reduced pressure) $= P_{chamber}/P_{cr}$. Froude number values were calculated at each chamber pressure to examine the importance of buoyancy forces within the distances investigated in this study. This number ranges from 42,000 to 110,000. Chen and Rodi (1980) suggested that the flow is momentum dominated when a defined length scale $x_b < 0.53$, while Papanicolaou and List (1988) suggested $x_b < 1$. Considering the more conservative estimate by Chen and Rodi (1980), the jet used here is momentum dominated for distances less than 30 to 40 mm from the injector exit. Pictures presented here cover up to about 5.5 mm (axial distance/diameter ratio of 21.6) from the injector and hence

buoyancy effects can be ignored in favor of the inertial forces.

The bottom row of Fig. 2 shows the jet shear layer. Generally, it is apparent that as pressure is increased, the jet width increases and the structure of the shear region changes from being dominated by ligaments and droplets to being dominated by finger-like structures. The results presented here are not unique to the injection of liquid nitrogen. Similar results have been found injecting liquid oxygen into gaseous nitrogen. In column (a), where the chamber pressure is subcritical, the jet has a classic liquid-like appearance. Consistent with the classical liquid jet breakup regimes described by Reitz and Bracco (1979), surface instabilities grow downstream from the injector and very fine ligaments and drops are ejected from the jet. This has been confirmed to correspond to the second wind-induced liquid jet breakup regime in Reitz and Bracco (1979).

Major structural and interfacial changes occurred at $P_r = 1.03$. Above this P_r, drops are no longer detected and regular finger-like entities are observed at the interface. Rather than breaking up into droplets, the interface dissolves at different distances from the dense core. These structures are illustrated at a $P_r = 1.22$ in column (b) of Fig. 2. This change in the morphology of the mixing layer is evidently due to the combined effects of reductions in the surface tension as the critical pressure is exceeded and enthalpy of vaporization because of this transition.

As chamber pressure is further increased, the length and thickness of the dense core decreased, and the jet begins to appear similar to a turbulent gaseous jet injected into a gaseous environment. This is illustrated in column (c). Any further droplet production, and consequently any additional classical liquid atomization, are completely suppressed.
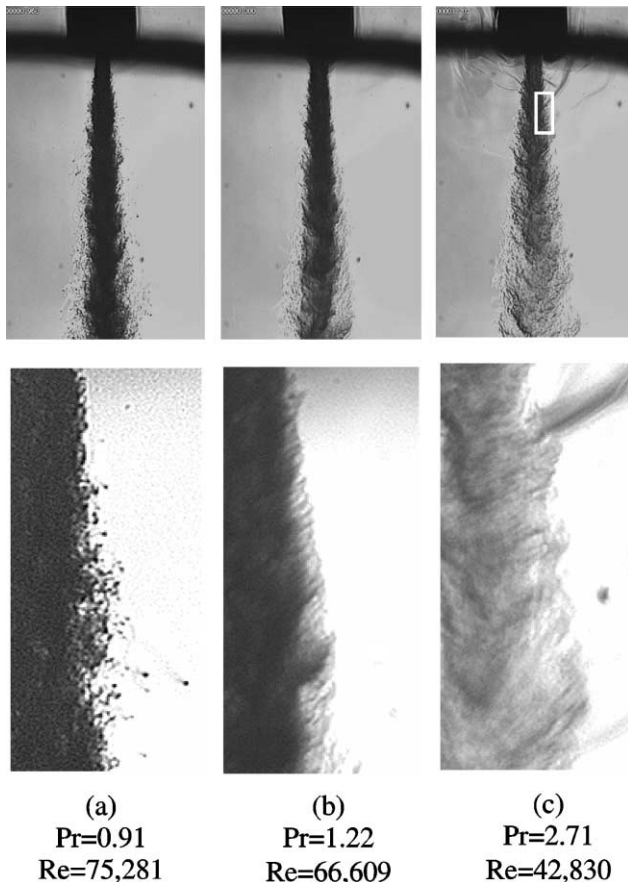
4. Jet and shear layer growth rates

In order to compare with classical mixing layer theory, the initial growth rate of the jets was measured at distances less than 28 jet diameters from the exit. As discussed by Chehroudi et al. (2002), this distance was well within the mixing layer region. The results were then plotted in Fig. 3 as the tangent of the spreading angle versus the chamber-to-injectant density ratio. Overlaid on top of the present data are the results of other researchers. Note that the jet studied here exhibits a dual character personality, liquid-like and gas-like. When liquid-like, it atomizes and produces a fine liquid droplet spray. However, consistent with other researchers, such a behavior is not detected and the jet resembles a gaseous jet injected into a gaseous environment under supercritical ambient pressure. Observing these two completely different characters motivated

(a)
Pr=0.91
Re=75,281

(b)
Pr=1.22
Re=66,609

(c)
Pr=2.71
Re=42,830

Fig. 2. LN_2 injected into room temperature nitrogen at different pressures. The bottom row contains magnified images of the top row in order to examine the shear layer.
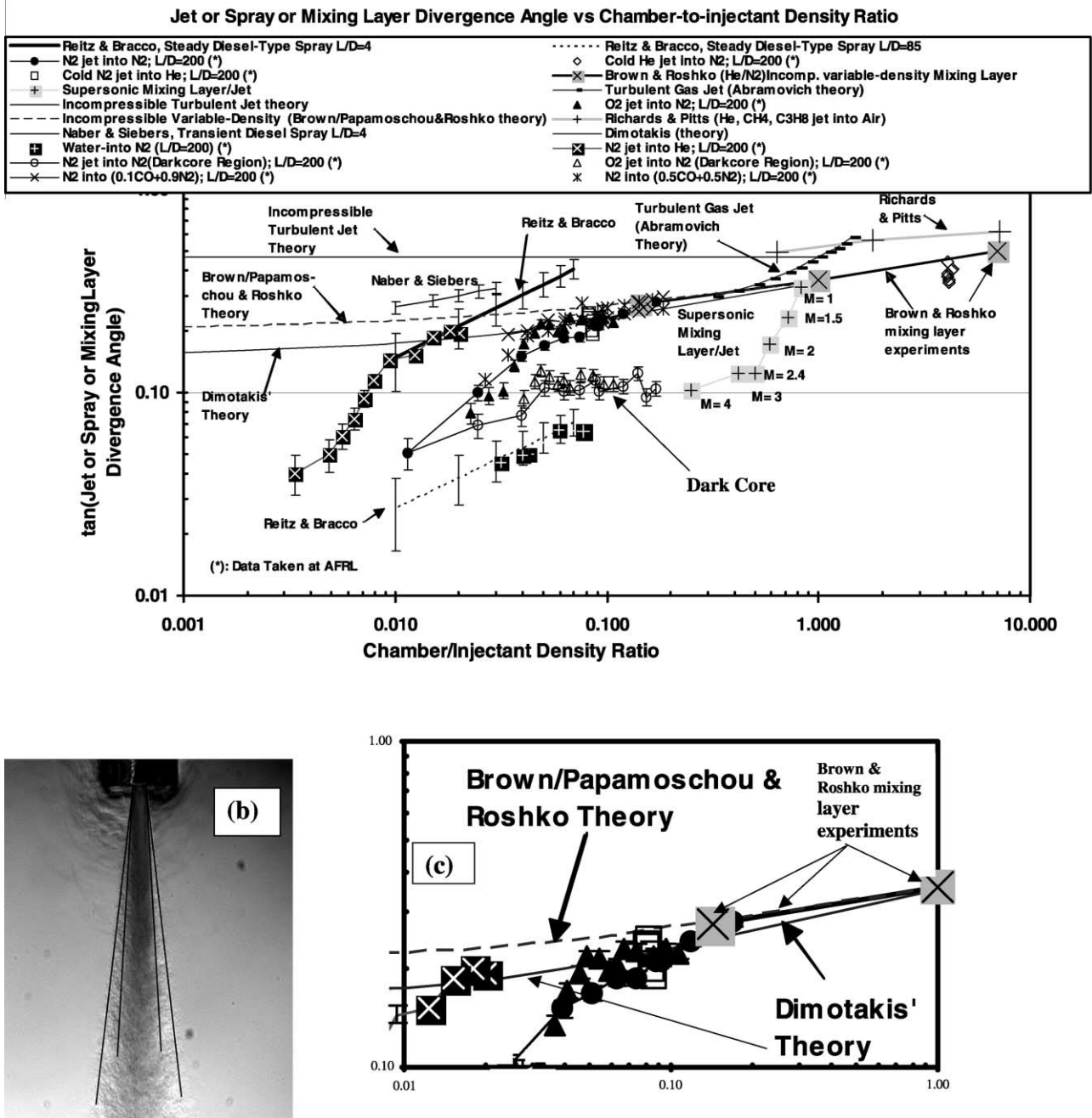
Fig. 3. (a) Spreading or growth rate as tangent of the visual spreading angle versus the chamber-to-injectant density ratio. (*) refers to data taken at AFRL. (b) An image of the jet depicting spread angle and dark-core angle measurements under high ambient pressure. (c) Plot is similar to (a) showing magnified data near the critical point.

us to simultaneously present "visual" spread rate for both liquid sprays (two-phase flow) and gaseous jets/mixing layers (single-phase flow). With the exception of the supersonic jet (shown for completeness) and incompressible gas jet theories (used as a reference), we selected those information found in the literature that are closest and of immediate relevance to the present case. All the data presented in this plot share the following attributes: straight-hole injectors, sufficiently-long nozzle hole length-to-diameter ratio (to ensure

fully-developed flow before the injector exit plane), Reynolds number range, momentum-dominated jets in the initial measurement zone, turbulent jet, comparable measurement zone for the growth rate, and consideration of the "visual" growth rate (all other growth rates were converted to "visual" rates). This resulted in a plot that is unique in that it spans nearly four orders of magnitude in density ratio and compares growth rates for both two-phase liquid sprays and single-phase turbulent jets.

We will first examine the subcritical region of Fig. 3. A more complete description can be found in Chehroudi et al. (2002). In this region, the LN_2 jet appears visually to have spray-like characteristics, as seen in Fig. 2a. The growth rate of this jet approaches the trend of that seen in liquid spray measurements such as Reitz and Bracco (1979), shown in Fig. 3. Their results represent the predictions of the linear stability atomization theory, while the error bars represent the extent of experimental scatter around the theoretical predictions. Results by Naber and Siebers (1996) are also shown for comparison purposes. Reitz and Bracco's data show the well-known result that the initial spreading rates of sprays from plain round orifices are sensitive to the injector internal geometry and, in particular, to the injector hole parameter, L/d_e. However, in comparing the shape of the curves, their data for $L/d_e = 85$ closely correspond to the LN_2 jet data at $L/d_e = 200$. In both of these cases, the flow is fully developed. As the density ratio is increased into the transition region (as seen in Fig. 2b), the jet and shear layer growth rate also increases. Near the critical pressure, the rate of increase becomes much steeper. Note that the abrupt change occurs at different density ratios for the different data sets in Fig. 3 because the data sets correspond to different mixtures with different critical properties.

At supercritical chamber pressures, where the LN_2 jet visually resembles a turbulent gas jet, the growth rate closely follows both the theoretical equation proposed by Dimotakis (1986) and the independently-derived equation by Papamoschou and Roshko (1988) for incompressible variable-density mixing layers. The spreading angle of the jet shear layer also agrees with Brown and Roshko's (1974) spreading angle measurements of an incompressible variable-density turbulent mixing layer between helium and nitrogen gases. Comparison with mixing layer data is justified because our measurements are within the initial mixing layer of the jet and do not extend far beyond the length of the potential core (for single-phase gaseous or liquid jets) and the intact core (for two-phase liquid sprays), see Chehroudi et al. (2002, 1999).

These growth rate measurements complement and extend the visualization results of the previous section. At supercritical pressures, not only do the jets have the visual appearance of a turbulent gas jet, but also the growth rates measurements are consistent with incompressible variable-density turbulent jets. This quantitative agreement was first shown in Chehroudi et al. (1999). At subcritical pressures, the jets have the same appearance and growth rate trend as liquid sprays. The transition between the two regimes occurs near the critical pressure. The above conclusions have been demonstrated for the case of a fully-developed flow at the jet exit. Other initial conditions have not yet been examined.

5. Fractal analysis

The notion of a fractal has been given a strong foundation and application by its father Mandelbrot (1983). Fractals are intimately connected to the concept of self-similarity. In essence, a similarity transformation involves one or combination of multiplication by a scale factor, pure translation, and pure rotation. Under such a transformation a geometrical object stays similar to the original or to a preceding stage if repetitively applied. Self-similarity, however, in a strict sense means that if one chooses any point of a geometrical object and locally magnifies, it will look similar to the "whole" object. In a sense infinite number of the scaled-down version of the "whole" are embedded in the "whole." In nature such idealized mathematical objects do not exit. For example, Peitgen et al. (1992) explain that a cauliflower head contains branches or parts, which when removed and compared with the whole are very much the same, only smaller. Applying the proper scale factor, the head and the branches are identical. These can again be decomposed into smaller ones, which again look very similar to the whole as well as to the first generation branches. This self-similarity carries through for about three to four stages, unlike the mathematical fractals which can be decomposed an infinite number of times. After that the structures are too small for a further dissection. Hence, in natural geometrical constructs self-similarity is confined between two sizes (or scales) referred to as inner (the smallest size) and outer cut-offs (the largest size).

The fractal dimension of any curve is between 1 and 2. The more wrinkled and space-filling the curve, the larger the value of the fractal dimension. Natural curves, similar to a cauliflower, are self-similar only to within a narrow range of scales. Our objective here is to measure the fractal dimension of the interface of the jets injected into the chamber to see if any pattern is uncovered. To our knowledge, this is the first application of the fractal approach to the liquid jet interface under sub- and supercritical conditions.

The fractal dimension of jets at various pressures ranging from subcritical to supercritical was calculated and compared to results of other researchers. Reference results were taken from Sreenivasan and Meneveau (1986) who measured the fractal dimensions of a variety of turbulent gaseous jets, mixing layers and boundary layers. These results indicate a fractal dimension between 1.33 and 1.38. In addition, the fractal dimensions of a turbulent water jet (Dimotakis et al., 1983) and of a liquid jet in the second wind-induced atomization regime (Taylor and Hoyte, 1983) were computed from high-resolution scanned images.

The fractal dimensions from the above reference cases are shown as horizontal lines in Fig. 4. Overlaid on top of these lines are discrete points indicating the fractal

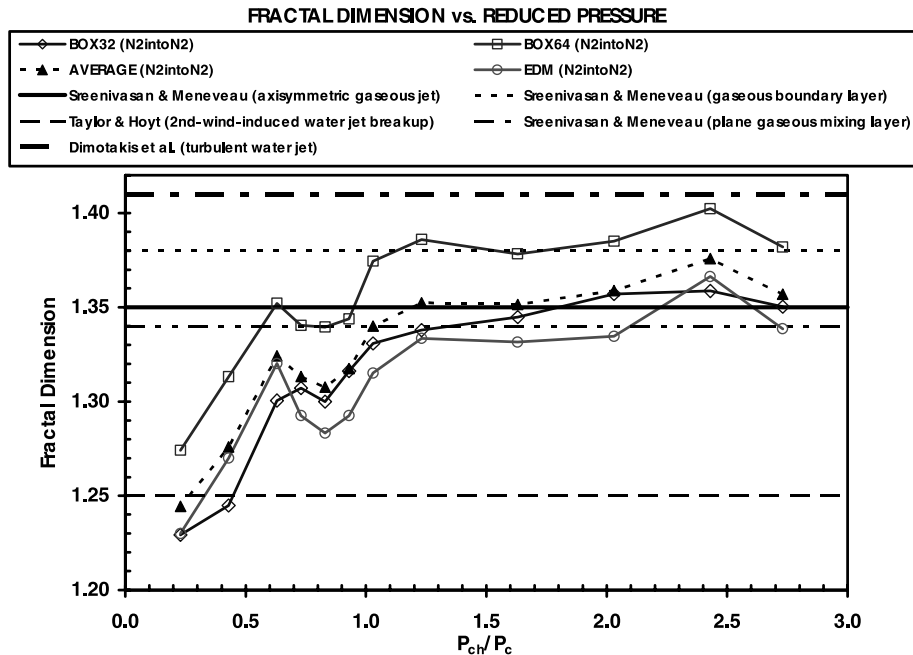**FRACTAL DIMENSION vs. REDUCED PRESSURE**

Fig. 4. Fractal dimensions of the boundaries of various jets as a function of reduced pressure (chamber pressure divided by the critical pressure of the jet material). Discrete points are data from the present study. Box32, Box64, and EDM are different methods of calculating the fractal dimension, giving an impression of the extent of variability, for details see Chehroudi et al. (1999).

dimension of LN_2 jets injected into GN_2 at various chamber pressures. At supercritical chamber pressures, the fractal dimension approaches a value similar to gaseous turbulent jets and mixing layers. As the chamber pressure is decreased, the fractal dimension also decreases. Below $P_r = 0.8$, the fractal dimension rapidly reduces to a value approximately equal to that of a liquid spray in the second wind-induced liquid jet breakup regime.

A more thorough discussion of the above results is found in Chehroudi et al. (1999). The key observation to be taken is that the results from the fractal analysis complement and extend the previous results. At supercritical pressures, jets have a fractal dimension similar to turbulent gas jets, and at subcritical pressures, cryogenic jets have a fractal dimension similar to liquid sprays. The transition occurs at about the same pressure as the transition in visual appearance and growth rate.

6. Modeling the growth rate

Using the data collected on the growth of the cryogenic jet, a phenomenological model for the growth rate has been developed. Complete details about the development of this equation are given in Chehroudi et al. (1999). The physical reasoning motivating the equation is outlined below. It was noticed that previous expressions for the growth rate of liquid sprays and of turbulent jets have a remarkably similar form. Reitz and

Bracco (1979) proposed that the growth rate of an isothermal steady liquid spray could be expressed as

$$\theta \approx 0.27[0 + (\rho_g/\rho_l)^{0.5}].$$

The first term in the bracket is the number zero to contrast with other equations discussed next. Similarly, Papamoschou and Roshko (1988) suggested the following form for incompressible, but variable-density, turbulent gaseous jets:

$$\theta = 0.212[1 + (\rho_g/\rho_l)^{0.5}].$$

The similarity in the form of these equations suggests the potential for a link between the two. Imagine a jet that is being injected into a subcritical pressure environment similar to the ones shown in Fig. 2. Clearly there are drops and ligaments, testifying the existence of a surface tension. Also evidence of a phase change is seen. Hence, one appropriate characteristic time of the problem (at subcritical, $P_r < 1$) is the "bulge" formation/separation time (τ_b) on the interface of the turbulent liquid jet. This time characterizes the formation and separation event of bulges from the liquid jet producing isolated ligaments and drops. Tseng et al. (1995) suggest that this time is equal to $(\rho_l L^3/\sigma)^{1/2}$ for the primary breakup of turbulent liquid jets where ρ_l, L, and σ are liquid density, characteristic dimension of turbulent eddy, and surface tension, respectively. The second relevant characteristic time (at subcritical) is the gasification time (τ_g). Here, an estimate of this time is calculated through the so-called D-square law for drops to be equal

to D^2/K where D and K are drop diameter and vaporization constant, respectively. In addition, we also propose the following hypothesis. If the aforementioned characteristic times (calculated for appropriate length scales) are nearly equal in magnitude then the interface bulges are not able to separate as unattached entities from the jet interface to form ligaments and drops because they are gasified as fast as they desire to be detached. Here, this is defined as the onset of the gas-jet like behavior. Therefore, the transition between liquid-like and gas-like behavior would be governed by finding the point at which these time scales are approximately equal. This is suggested by the comb-like structures seen in Fig 2(b).

Using the above physical models, an equation was proposed for the N$_2$/N$_2$ system as

$$\theta = 0.27[\tau_b/(\tau_b + \tau_g) + (\rho_g/\rho_l)^{0.5}].$$

In the limit, when $\tau_g \gg \tau_b$ and $\tau_g \to \infty$, this equation collapses to the isothermal liquid spray case. This equation agrees well with the current data at subcritical pressures for $\tau_b/(\tau_b + \tau_g) < 0.5$. A constant value of 0.5 was used to predict the spreading rate for higher pressures, including supercritical pressures.

For injection of N$_2$ into N$_2$, the characteristic time ratio, $\tau_b/(\tau_b + \tau_g)$, was calculated from experimental measurements of bulge and droplet sizes and calculations of the relevant properties. For N$_2$ injection into other gases, however, reliable information about the mixture properties at the interface, particularly the surface tension, prevents such a calculation from being performed. To model these cases, it is hypothesized that the characteristic time ratio is a dominant function of the density ratio, i.e. $\tau_b/(\tau_b + \tau_g) = F(\rho_g/\rho_l)$. Brown and Roshko (1974), indicate that this hypothesis is reasonable because at low Mach numbers there is no distinction between mixing layers where the two streams have different molecular weights, temperatures, or compressibility effects. Measurements and calculations of $\tau_b/(\tau_b + \tau_g)$ provides the shape of the function F for the N$_2$/N$_2$ system and is provided as a plot in Chehroudi et al. (1999). A curve fit of that plot gives

$$F(\rho_g/\rho_l) = 5.325(\rho_g/\rho_l) + 0.0288 \quad \rho_g/\rho_l < 0.0885$$
$$= 0.5 \quad \rho_g/\rho_l \geqslant 0.0885$$

It was found that the same function, F, calculated from measurements of the N$_2$/N$_2$ system could be made to work for other cases, provided that a case-dependant transformation was made to the density ratio at which F is evaluated. The final form of the equation thus arrived at is

$$\theta = 0.27[F(x(\rho_g/\rho_l)) + (\rho_g/\rho_l)^{0.5}],$$

where, $x = 1.0$ for N$_2$-into-N$_2$, $x = 0.2$ for N$_2$-into-He, and $x = 1.2$ for N$_2$-into-Ar.

In other words, the same functional form of the characteristic time ratio, $\tau_b/(\tau_b + \tau_g) = F(\rho_g/\rho_l)$, for the N$_2$-into-N$_2$ case is used but with a density-ratio coordinate transformation. The quality of the agreement with experimental data is demonstrated in Fig. 5. Hence there are no major changes in the form of the proposed
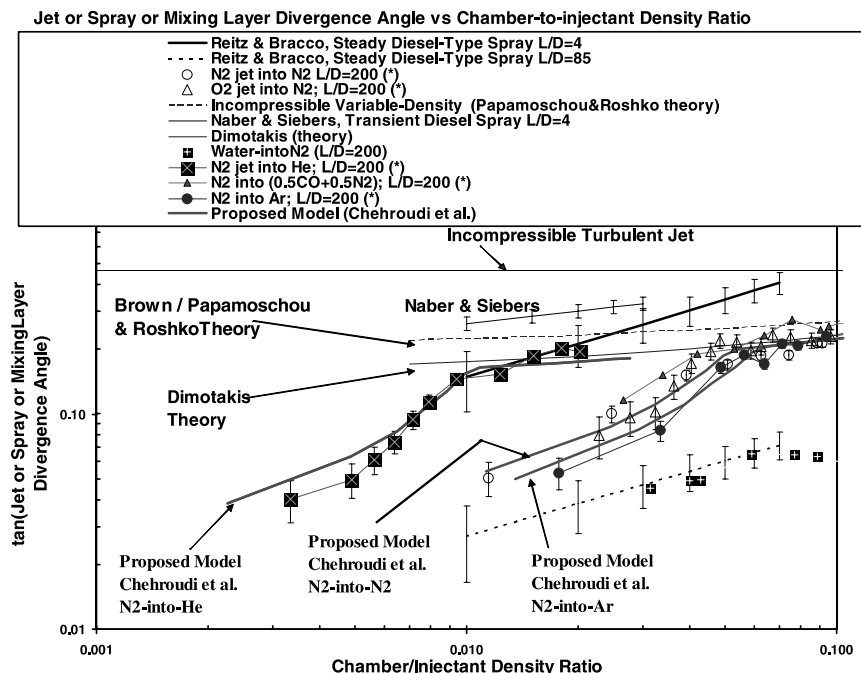

Fig. 5. Comparison of the proposed growth rate model by Chehroudi et al. (1999) with experimental data.

model equation even for as extreme of an arrangement as injection of N_2 into He. However, an observation is made here. The factor $x = 0.2$ in the N_2-into-He case is comparable to the molecular weight ratio of He to N_2 of 0.14, while the factor $x = 1.2$ in the N_2-into-Ar case is comparable to the molecular weight ratio of 1.42. This also suggests the dominant effect of the density ratio parameter between the cases.

7. Raman scattering measurements

In addition to the line-of-sight shadowgraph images from which the preceeding results have been acquired, spontanenous Raman scattering has also been used to obtain spatially-resolved measurements of the density distribution within the cryogenic jet. Raman scattered light results from an inelastic collision between light photons and molecules. Since the process is inelastic, the incident beam will be shifted a fixed amount dependent upon the structure of the molecule. Generally, the intensity of the Raman scattered signal yields information on the number density of the gas being examined. The Raman spectra are obtained by irradiating a sample with a powerful visible monchromatic source. The scattered signal is usually observed at 90° to the incident beam with a suitable visible-region detector or spectrometer. The scattered radiation does not exceed 0.001% of the source, as a result detection and measurement is difficult except for the resonant Raman. The scattered light is of three types, Stokes, anti-Stokes, and Rayleigh. Rayleigh, which has exactly the same frequency as the excitation source, is substantially more intense than either two. Stokes peak lines are found at wavelengths larger (lower energies) than the Rayleigh peak while anti-Stokes are at smaller (higher energies) than the wavelength of the source. It is critical to realize that the magnitude of the Raman shifts are independent of the wavelength of excitation source. A more detailed description of these experiments and Raman effect can be found in Chehroudi et al. (2000).

Fig. 6 shows typical averaged raw images of the LN_2 jet at sub- and supercritical conditions. The Raman intensity profile for the subcritical case is larger in magnitude at the center of the jet and is narrower in shape than the corresponding image of the supercritical jet. The observed Raman intensity radial profile broadening prevented us from using the jet thickness definition proposed by Brown and Roshko (1974) based on the 1% free stream density point on the radial profiles. Instead, the full-width of the radial profiles measured where the intensity increment was half the maximum (Full-Width-Half-Maximum, FWHM) appeared a safer parameter for comparison with other results. Also, it is not known if density values can be measured to within 1% accuracy. Nevertheless, Brown and Roshko (1974) reported that
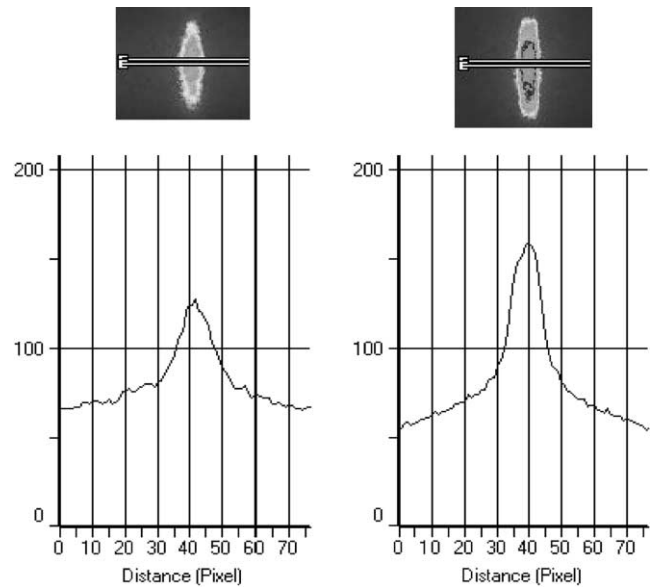

Fig. 6. Averaged Raman images of LN_2 jet (flowing downward) at sub- and super-critical chamber conditions. Raman intensity radial profiles (radial direction is quantified by pixels) are also shown. Left: Chamber pressure of 6.9 MPa (supercritical); right: chamber pressure of 1.46 MPa (subcritical).

their 1% thickness definition corresponded fairly well with the extent of the mixing visible on the shadowgraph pictures. The FWHM was extracted from the measured Raman data, and the spreading rate thus measured was compared with the spreading rate measured from the shadowgraph visualizations. The results are plotted in Fig. 7. It was found that the spreading rate measured at twice the FWHM values of the Raman data agreed well with the shadowgraph measurements. Thus the correspondence of the two different techniques of measuring the width of the jet was established.
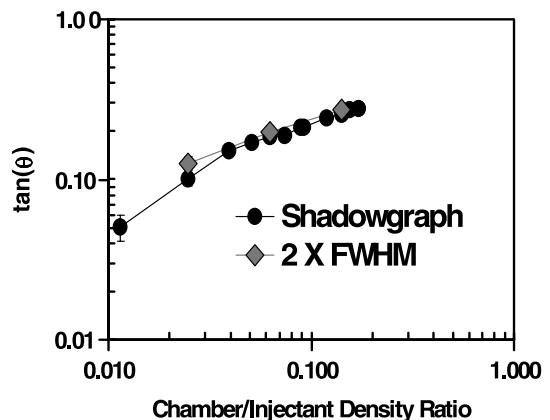

Fig. 7. Comparison of the tangent of the spreading angle measured using shadowgraph and Raman techniques using twice the FWHM values.

8. Summary and conclusions

The structure and initial growth rate of cryogenic jets injected into an ambient with a pressure which ranged from subcritical to supercritical have been studied at AFRL. At subcritical pressures, comparison of shadowgraph measurements show that the jets have the appearance of a conventional liquid spray. As pressure is increased beyond the injected fluid critical pressure, the structure of the jet changes. Under these conditions, the cryogenic jets have the appearance of turbulent gaseous jets. Quantitative agreement of the jet initial growth rate measurements with those predicted by the theoretical equations and measurements for incompressible variable-density gaseous jets has been shown for the first time. Also, for the first time, a unique plot has been generated through conversion of all growth rate types to the "visual" growth rate using the most relevant works reported by other researchers on variable-density incompressible mixing layers, axisymmetric incompressible and compressible gas jets, supersonic jets/mixing layers, and liquid sprays. The resulting plot of spreading angle as a function of density ratio spans four orders of magnitude in density ratio.

A physically-based phenomenological model was developed which proposes a mechanism governed by the characteristic gasification times and interfacial turbulent bulge formation times to predict the measured growth rate behavior. Spontaneous Raman scattering measurements of the density have been used to confirm the earlier shadowgraph measurements. Growth rate measurements derived from the Raman measurements at twice the FWHM distance correspond very closely to the growth rate derived from the shadowgraph measurements.

Acknowledgements

References

Anderson, T.J., Woodward, R.D., Winter, M. 1995. Oxygen Concentration Measurements in a High Pressure Environment Using Raman Imaging, AIAA Paper 95-0140, 33rd Aerospace Sciences Meeting and Exhibit, January 9–12, Reno, NV, 1995.

Brown, G., Roshko, A., 1974. On density effects and large structure in turbulent mixing layers. J. Fluid Mech. 64 (4), 775–816.

Bruno, T.J., Ely, J.F., 1991. Supercritical fluid technology: review in modern theory and applications. CRC Press, Boca Raton.

Chehroudi, B.R., Cohn, R., Talley, D., Badakhshan, A. 2000. Raman scattering measurements in the initial region of sub- and supercritical jets. AIAA Paper 2000-3392.

Chehroudi, B., Talley, D.G., Coy, E.B., 2002. Visual characteristics and initial growth rates of round cryogenic jets at subcritical and supercritical pressures. Phys. Fluids 14 (2), 850–861.

Chehroudi, B., Talley, D.G., Coy, E.B. 1999. Fractal geometry and growth rate of cryogenic jets near critical point. AIAA paper 99-2489.

Chen, C.J., Rodi, W., 1980. Vertical turbulent buoyant jets—a review of experimental data. Pergamon, New York.

Decker, M.C., Schik, A., Meier, U.E., Stricker, R.W., 1998. Quantitative raman imaging investigations of mixing phenomena in high pressure cryogenic jets. Appl. Opt. 37, 5620–5627.

Dimotakis, P.E., 1986. Two-dimensional shear-layer entrainment. AIAA J. 21 (11), 1791–1796.

Dimotakis, P.E., Miake-Lye, W.G., Papantoniou, D.A., 1983. Phys. Fluids 26, 3185.

Mandelbrot, B.B., 1983. The Fractal Geometry of Nature. W.H. Freeman and Company, San Francisco.

Mayer, W., Schik, A., Schweitzer, C., Schaffler, M. 1996. Injection and mixing processes in high pressure LOX/GH2 rocket combustors, AIAA Paper no. 96-2620, 32nd AIAA/ASME/SAE/ASEE Joint Propulsion Conference & Exhibit, Lake Buena Vista, Florida.

Mayer, W., Ivancic, A., Schik, A., Hornung, U. 1998. Propellant atomization in LOX/GH2 rocket combustors, AIAA Paper no. 98-3685, 34 the AIAA/ASME/SAE/ASEE Joint Propulsion Conference & Exhibit, Cleveland, Ohio, July 13–15.

Naber, J.D., Siebers, D.L. 1996. Effects of gas density and vaporization on penetration and dispersion of diesel sprays, SAE Paper no. 960034.

Newman, J.A., Brzustowski, 1971. Behavior of a liquid jet near the thermodynamic critical region. AIAA J. 9 (8), 1595–1602.

Oschwald, M., Schik, A., 1999. Supercritical nitrogen free jet investigated by spontaneous Raman scattering. Exp. Fluids 27, 497–506.

Oschwald, M., Schik, A., Klar, M., Mayer, W. 1999. Investigation of Coaxial LN2/GH2-Injection at Supercritical Pressure by Spontaneous Raman Scattering, 35th AIAA/ASME/SAE/ASEE Joint Propulsion Conference and Exhibit, Los Angeles, CA, 20–24 June.

Papamoschou, D., Roshko, A., 1988. The compressible turbulent shear layer: an experimental study. J. Fluid Mech. 197, 453–477.

Papanicolaou, P.N., List, E.J., 1988. Investigations of round vertical turbulent buoyant jets. J. Fluid Mech. 195, 341–391.

Peitgen, H.-O., Hartmut, J., Dietmar, S., 1992. Fractals for the Classroom, Part one Introduction to Fractals and Chaos. Springer-Verlag New York Inc, New York.

Reitz, R.D., Bracco, F.V. 1979. On the dependence of spray angle and other spray parameters on nozzle design and operating condition, SAE Paper no. 790494.

Sreenivasan, K.R., Meneveau, C., 1986. The fractal facets of turbulence. J. Fluid Mech. 173, 357–386.

Taylor, J.J., Hoyte, J.W., 1983. Water jet photography-technique and methods. Exp. Fluids 1, 113–120.

Tseng, L.-K., Ruff, G.A., Wu, P.-K., Faeth, G.M. 1995. Continuous- and dispersed-phase structure of pressure-atomized sprays. Progress in Astronautics and Aeronautics: Recent Advances in Spray Combustion, February, 1995.

Woodward, R.D., Talley, D.G. 1996. Raman imaging of transcritical cryogenic propellants, AIAA paper 96-0468.